Journal of
Materials Chemistry A

ROYAL SOCIETY
OF CHEMISTRY

PAPER

View Article Online
View Journal | View Issue

Check for updates

Cite this: *J. Mater. Chem. A*, 2021, **9**, 16917

Received 20th March 2021
Accepted 20th July 2021

DOI: 10.1039/d1ta02352g

rsc.li/materials-a

An EPR investigation of defect structure and electron transfer mechanism in mixed-conductive $LiBO_2–V_2O_5$ glasses†

Jacob N. Spencer, *[a] Andrea Folli, [a] Hong Ren[b] and Damien M. Murphy *[a]

Continuous Wave (CW) Electron Paramagnetic Resonance (EPR) spectroscopy was used to study the defect structure and electron transfer mechanism in a series of $LiBO_2–V_2O_5$ mixed conductive glasses of varying V_2O_5 content. These glassy materials are attracting growing interest for energy storage devices. At low V_2O_5 content (VLB1), an isolated $S = \frac{1}{2}$ vanadium defect centre is found at a network modifying position within the $LiBO_2$ matrix. The observed spin Hamiltonian parameters are consistent with a V^{4+} centre possessing a distorted octahedral configuration and d_{xy} orbital ground state. At high V_2O_5 content (VLB3), the vanadium hyperfine structure is absent indicative of a distinct exchange-narrowed signal. A model was developed to analyse the linewidth and g-tensor component of the EPR signals, revealing a marked temperature dependent behaviour, consistent with a polaron hopping mechanism of electron transfer and inter-electronic exchange along the g_3 direction, coincident with the electron transfer axis. The activation energy (E_a) was estimated to be 0.081 eV, consistent with other conducting glasses. A relaxation-dominated line broadening mechanism was further supported by multi-frequency EPR measurements, which also identified unresolved features at high frequencies due to unaccounted for anisotropic exchange/speciation within the disordered network. This analysis provides a straight-forward method for the use of EPR to investigate solid-state glassy materials.

Introduction

The tuneable multi-functional properties of V_2O_5-based materials have led to its incorporation in a variety of energy storage, optical and electrocatalytic applications (especially as water-splitting cathodes).[1–4] Amorphous vanadate glasses are also attractive for use as solid state electrolytes,[5–10] cathodes for Li-ion batteries,[11,12] and alternative alkali-ion battery technologies,[13–15] due primarily to the content-dependent mixed ionic-electronic conductivity of the materials. Vanadium possesses multiple accessible redox couples, which provides a subsequent high theoretical capacity and energy density that can incorporate up to three Li ions per V_2O_5 unit.[11] Crystalline V_2O_5 materials have had limited commercial application due to the poor capacity retention, which results from irreversible phase changes (amorphisation) and volume expansion upon Li incorporation. On the other hand, amorphous vanadate materials have been shown to reduce some of these challenges and therefore offer a highly attractive route that overcomes performance-limiting properties upon intercalation.

The functional properties of these glassy materials are highly dependent on the nature and content of the precursors used in their preparation. A great deal of literature is available that focuses on the structural characterisation of V_2O_5-based glassy materials for a variety of applications.[14,16–19]

For example, when V_2O_5 behaves as a network modifier, *i.e.*, at low contents, its incorporation into a borate network can be accompanied by a modification of the regular (trigonal) structure as diborate, chain-type metaborate and tetrahedral BO_4 units.[20] The presence of trigonal and tetrahedral borate sites was also confirmed in other studies of $xV_2O_5(1-x)[2B_2O_3–Li_2O]$ glasses[21] closely analogous to the glass samples to be reported in this study.

Glasses containing high V_2O_5 content (up to $x = 0.8$; $xV_2O_5(1-x)B_2O_3$) were also described in the literature,[20] where V_2O_5 acts as a network former, and revealed that borate was only present as tetrahedral BO_4^- units in network modifying positions. At V_2O_5 contents greater than the $LiBO_2$ contents, vanadium can also be considered the primary network former and therefore, to local order, can be a useful model in the characterisation of the V^{4+} defects in amorphous materials. The electronic interactions between V^{4+} defects actually mediate the polaron hopping mechanism of electron transfer for conductivity (Fig. 1). The local defect structure, primarily vacancies and

---

[a]School of Chemistry, Cardiff University, Main Building, Park Place, Cardiff CF10 3AT, UK. E-mail: jacob0spencer@outlook.com; MurphyDM@cardiff.ac.uk

[b]Johnson Matthey Technology Centre, Blounts Court Road, Sonning Common, Reading, Berkshire RG4 9NH, UK

† Electronic supplementary information (ESI) available. See DOI: 10.1039/d1ta02352g

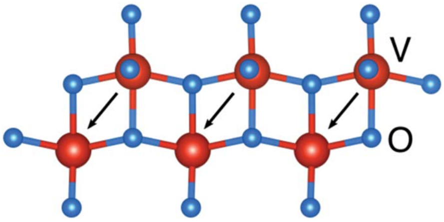

Fig. 1 Schematic illustration of polaron hopping direction in a V_2O_5 type phase.

cationic impurities (such as Li), are then generally responsible for the formation of the V^{4+} sites.

The introduction of oxygen vacancies into V_2O_5 can also induce ferromagnetism between sites of the form $V_2O_{(5-x)}$ (where $x < 0.13$ and $0.19 < x < 0.45$), with the electron spin density occupying a $3d_{xy}$ orbital ground state.[22] These electrons are then spin polarised due to intra-atomic exchange interactions giving rise to half-metallic ferromagnetism. Other theoretical and experimental studies have also shown that for higher oxygen vacancy concentrations ($x > 0.45$), anti-ferromagnetic ordering can dominate.[23]

This presents a straight-forward model upon which the effect of incorporation of network modifying defects, such as Li and B, in addition to intrinsic defects such as oxygen vacancies, can be understood in terms of their resulting magnetic properties. The formation of intrinsic oxygen vacancies that can lead to V^{4+} defects can occur through charge compensation according to:[24]

$$2V_V^{\times} + O_O^{\times} \rightleftarrows 2V_V^{'} + \square_O^{\cdot\cdot} + \frac{1}{2}O_2 \tag{1}$$

and in this case, the intrinsic concentration of oxygen vacancies is approximately equal to half the concentration of V^{4+}.[24]

A useful comparison for the vanadate glass network is the understanding of Li-defect chemistry in the V_2O_5 network, particularly the electrochemical insertion of Li-ions.[25] Introduction of Li^+ into a V_2O_5 intercalation site is accompanied by the reduction of a single V^{5+} site to V^{4+} and association to the adjacent oxygen site forming a coupled electron–hole pair:

$$V_V^{\times} + O_O^{\times} + Li^+ + e^{'} = V_V^{'} + OLi_i^{\cdot} \tag{2}$$

where $V_V^{\times}$ denotes the V^{5+} site, $O_O^{\times}$ is an O^{2-} site, $V_V^{'}$ is an effective V^{4+} defect site and $OLi_i^{\cdot}$ is the associated oxygen site with intercalated Li^+ and a net positive charge.

It is clear that the electrochemical stability and performance of the electrode materials is directly related to the local electronic structure of the redox-active vanadium sites, in addition to defects, vacancies, dislocations *etc.* as a result of the disordered glassy network. Amorphous glasses can hence present challenges in understanding the local structure of the material due to short-range order and localised ordering. Information from conventional techniques for structural determination, such as XRD, can often be challenging in providing a comprehensive structural view of the material.

By comparison, EPR spectroscopy can be readily exploited as a powerful characterisation technique when studying such glassy materials bearing paramagnetic vanadium states, notably V^{3+} ($S = 1$; $^3F_4$) and V^{4+} ($S = 1/2$; $^2D_{5/2}$).[26] The compressed octahedral oxovanadium(IV) or vanadyl ion, VO^{2+}, is a common paramagnetic site in glass systems containing V_2O_5, which is often used as a structural probe for EPR investigation.[27–29] The coordination environment is critical in determining the relative ordering of the 3d states and hence the orbital occupancy of the unpaired electron. Due to the orbital contribution to the total angular momentum, the *g*-tensor is also highly sensitive to its coordination environment. Furthermore, hyperfine and super-hyperfine interactions with neighbouring nuclei, offer a wealth of information on the local site symmetry, coordination and geometry.

It is important to note that in the glassy materials, two distinctly different and observable V^{4+} environments can be expected, with the vanadium acting as a network forming or network modifying phase.[30–32] At low contents, in the network modifying phase, V^{4+} defects are formed *via* charge compensation for Li and B, and can be considered well isolated in the bulk $LiBO_2$ network compared to other substitutional vanadium sites. On the other hand, in network forming phases, the structure is akin to defective V_2O_5 (to short range order), whereby V^{4+} sites are formed *via* incorporation of Li, B and oxygen vacancy defects. In this case, the spin delocalisation and spin concentration is much greater, and the V^{4+} defects can no longer be considered as isolated, localised species. This environment is then attributed to an extended lattice of interacting spins, responsible for the super-exchange behaviour associated with polaron hopping conductivity. The inequivalence of exchange pathways along the lattice dimensions is thus highly dependent on the local structure, and bonding to nearby spins, and hence the magnitude of the electronic interactions are sensitive to this. Both of these environments can be readily interrogated by EPR spectroscopy.

In this study we have therefore employed continuous wave (CW) EPR spectroscopy to investigate the electronic structure of V^{4+} sites and the inter-site interactions or relevance to electronic conductivity. A series of $LiBO_2$–V_2O_5 (VLB) glasses, varying in V_2O_5 content, were studied in order to identify the distinct $V_V^{'}$ and other defective sites present. Careful analysis of line width broadening in the EPR spectra provides insights into the exchange network and polaron hopping conduction afforded by defect formation and spin density delocalisation. The EPR line width analysis model adopted here affords an estimate of the polaron hopping activation energy, the Curie–Weiss temperature and the isotropic exchange integral. These parameters can in turn be used to directly probe the correlation of paramagnetic, redox-sensitive sites, and rationalise the local environment and functional properties of V_2O_5 based glassy materials.

Experimental

Materials and methods

All precursors were used as-received without further purification.

Synthesis

The V_2O_5–$LiBO_2$ glass materials studied in this work were prepared *via* a melt-quench method. Analytical pure grade raw materials *i.e.* V_2O_5 (≥99.6%, Aldrich) and $LiBO_2$ (99.9%, Alfa Aesar) were weighed according to the corresponding ratios of V_2O_5 to $LiBO_2$. The weighed raw material mixtures were thoroughly mixed using a Turbula Mixer for 45 minutes before they were placed in Pt crucibles and heated in a muffle furnace to 900 °C for 60 minutes. To prevent the crystallisation due to the slow cooling rate, homogeneous melts were poured directly into baskets containing liquid nitrogen. The produced ingots were then crushed and dry-milled using a high energy planetary mill. The homogeneous melts were milled using 20 mm diameter YSZ milling balls for 20 minutes, and subsequently milled with 3 mm diameter beads for 40 minutes. The full milling process gave rise to a fine powder to be characterised by EPR spectroscopy.

Continuous-wave (CW) EPR spectroscopy

The X-band (9 GHz) CW-EPR spectra were recorded at 120 K on a Bruker EMX spectrometer, operating at 100 kHz field modulation frequency, 0.6325 mW microwave power and 1 G modulation amplitude using an ER 4119HS cavity. Approximately 50 mg of each sample was packing into a 3.8 mm I.D. quartz cell for these X-band measurements. For Q-band measurements, the samples were individually packed into a 1.2 mm I.D. quartz cell. The Q-band (35 GHz) spectra were then recorded at $T = 10$ K on a Bruker E500 spectrometer operating at 100 kHz field modulation frequency, 0.005 mW microwave power and 1 G modulation amplitude, using a Bruker ER5106 QT-E resonator. Finally, for W-band measurements, the samples were packed into a 0.5 mm I.D. quartz cell. The W-band (95 GHz) spectra were recorded at $T = 20$ K and 300 K on a Bruker E600 spectrometer operating at 100 kHz field modulation frequency, 0.005 mW microwave power and 1 G modulation amplitude, using an E600-1021H TeraFlex resonator. Field calibration was performed using a BDPA standard at X-band, and the microwave frequency for spectra at W-band were adjusted accordingly by simultaneous fitting at the three microwave frequencies.

Variable temperature (VT) X-band EPR measurements were also performed on the high V_2O_5 content sample, namely VLB3, using a Bruker E500 spectrometer equipped with a ER 4119HS resonator and an Oxford instruments cryostat. A saturation study was recorded to ensure that the operating microwave power was not within the saturation limit. Field calibration was performed using a BDPA standard. The operating parameters were 100 kHz field modulation frequency, 0.6325 mW microwave power and 1 G modulation amplitude. EPR measurements in the temperature range $T = 120$–370 K were recorded on a Bruker EMX spectrometer equipped with a ER 4119HS resonator, as stated *vide infra*. The Q value was checked to ensure a similar environment for the separate temperature ranges.

Simulations and fitting

Spectral simulations were performed using the EasySpin toolbox in MATLAB developed at ETH Zurich.[33] The simulation models used to reproduce the experimental data are discussed in the later.

Results and discussion

CW EPR study of $LiBO_2$:V_2O_5 glasses

In the first instance, a series of $LiBO_2$:V_2O_5 glass samples with varying V_2O_5 contents including VLB1 (70 : 30 ratio), VLB2 (36 : 64) and VLB3 (20 : 80), were prepared and characterised by X-band CW EPR spectroscopy. The resulting experimental and simulated spectra for these three representative samples are shown in Fig. 2.

At low V_2O_5 contents (VLB1) the spectrum is characterised by a well resolved 8-line hyperfine pattern resulting from the interaction of the electron spin ($S = 1/2$) with the ^{51}V nucleus ($I = 7/2$). The spin Hamiltonian parameters extracted from the simulation for the V^{4+} centre were found to be $g = [1.9775\ 1.9819\ 1.9471] \pm 0.003$ and $^{51V}A = [152.1\ 180.5\ 520.1] \pm 5$ MHz (Table 1).

The relative magnitudes of the g- and A-tensor components $g_e > g_{xx}, g_{yy} > g_{zz}$ and $A_{zz} > A_{xx}, A_{yy}$ are typical for a $3d^1$ VO^{2+} species occupying a distorted (tetragonally compressed) octahedral environment of C_2-type or lower symmetry with a $3d_{xy}$ orbital ground state.[34–38] These g and A values are consistent with other vanadium doped glass systems,[21,31,39–43] although the symmetry is typically reported to be axial in the literature. We assume (in the absence of single crystal or quantum chemical calculations) that the principle axis frames for the g and A tensors are collinear. The shifts in g tensor components from the free spin value ($\Delta g = g - g_e$), usually represented as $\Delta g_{\parallel}/\Delta g_{\perp}$, are frequently reported for vanadyl species,[21,44–46] as the degree of tetragonal distortion in the system after Kivelson and Lee.[47] Considering the relatively small deviation in the g_1 and g_2 values (≈0.0025), an average value may be used to approximate a value

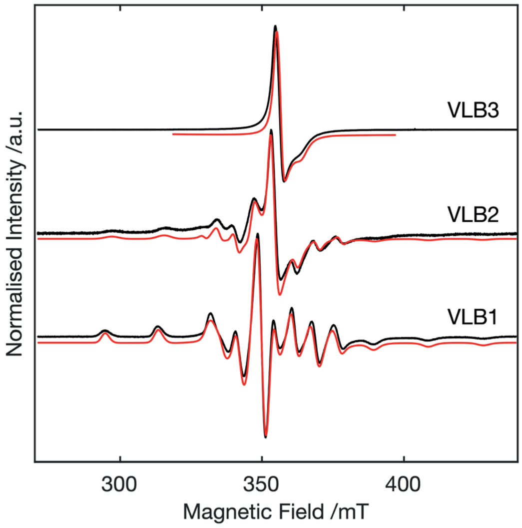

Fig. 2 Low temperature ($T = 120$ K) X-band CW EPR spectra of VLB1, VLB2, and VLB3 at varying V_2O_5 contents. The simulation for VLB3 was obtained using the simulation parameters derived from the variable frequency study *vide supra*. The homogeneous and inhomogeneous line widths for the g-components were varied by least-squares fitting to obtain the simulation at $T = 120$ K. *Black*: experimental spectrum; *red*: simulated spectrum.

Table 1 Spin Hamiltonian parameters for the V^{4+} species identified in amorphous vanadyl glasses, extracted by simulation of the experimental spectrum. All hyperfine related terms are given in MHz and are reported as magnitudes rather than absolute values. The full hyperfine tensor or respective isotropic and (total) anisotropic parts can be reconstructed using the identity matrices defined in eqn (1)

Species	g_{iso}	g		$\Delta g_{\parallel}/\Delta g_{\perp}$	a_{iso}	A		T^{c}		Symmetry
VO^{2+} (VLB1)	1.9688 ± 0.003	g_1	1.9775	2.44	284.2 ± 5	A_1	152.1	T (d_{xy})[d]	113.2, 122.7	Distorted O_h
		g_2	1.9819			A_2	180.5	T' (d_{nz})	9.45	
		g_3	1.9471			A_3	520.1			
VO^{2+} (VLB2)	1.9679 ± 0.003	g_1	1.9773	2.90	277.1 ± 5	A_1	134.8	T (d_{xy})[d]	106.3, 124.3	Distorted O_h
		g_2	1.9852			A_2	188.7			
		g_3	1.9411			A_3	507.7	T' (d_{nz})	18.0	
V_2O_5[a] (VLB3)	1.9720 ± 0.001	g_1	1.9925	4.13	N.R.[b]		N.R.[b]		N.R.[b]	Distorted sq. pyr.
		g_2	1.9825							
		g_3	1.9445							

[a] g tensor results were obtained from the simultaneous fitting of LBV3 at multiple frequencies (X, Q, W) and $T = 10$ K (X, Q) $T = 20$ K (W). [b] Not resolved. [c] Calculated solutions to the tensor composition into axial dipolar components, assuming A_3 coincides with the compressed axial direction. The values reported are magnitudes here are magnitudes (the relative sign cannot be determined). [d] The two solutions for T are given for completeness, dependent on the relative sign of T'.

Table 2 Fitting parameters and quantities obtained from linewidth analysis of VLB3

Component	E_a/eV	ΔB_0/mT	Θ_{CW}/K	J/cm^{-1}	a/mT K^{-1}
g_3	0.081	2.255	−16.8	−0.7928	−0.0161
$g_{1,2}$	0.094	1.390	−0.005	−0.0002	—

of $\Delta g_{\parallel}$ for simple comparison with similar vanadyl systems. The resulting values of $\Delta g_{\parallel}/\Delta g_{\perp} = 2.44$ and $\Delta g_{\parallel}/\Delta g_{\perp} = 2.90$ for VLB1 and VLB2 respectively, agree reasonably with other reported glasses containing similar phases.[21,44,47] A considerable increase in the value for VO^{2+} (VLB2), the network modifying vanadium defect in the intermediate content glass (VLB2), is consistent with a comparative increase in tetragonal distortion at the defect sites.

The full quasi-axial $^{51\mathrm{V}}A$ hyperfine tensor determined for VLB1 (Table 1) may be further analysed and decomposed into an isotropic (a_{iso}) component, and the sum of two traceless axial dipolar hyperfine tensors, following schemes related to the angular radial components for d_{xy} and d_{xz} orbitals reported by Morton and Preston:[48]

$$A_{ij} = a_{\mathrm{iso}} + \begin{bmatrix} T & & \\ & T & \\ & & -2T \end{bmatrix} + \begin{bmatrix} T' & & \\ & -2T' & \\ & & T' \end{bmatrix} \Big/ \mathrm{MHz} \quad (3)$$

In this case, one may obtain values of the anisotropic dipolar hyperfine terms, T and T', which correspond to $3d_{xy}$ and $3d_{nz}$ ($n = x,y$; the relative ordering cannot be determined) orbital states which admix *via* spin–orbit coupling. These relations reflect the localised electron spin density which partially occupies the next lowest lying $3d_{nz}$ orbital and suggests a destabilisation in the n-character orbitals through compression and/or strain.

In the absence of quantum chemical calculations, one may compare experimental values to the calculated atomic parameters,[48] in order to extract and estimate further information about the ground state electronic structure and spin density at the vanadium centre. The reported values for vanadium correspond to $A_0 = 4165$ MHz and $P = 437.6$ MHz,‡ in addition to the anisotropic angular factors required for the occupied orbital (2/7 for d_{xy} and d_{nz}). The A_3 component is assumed to be coincident with the compressed D_{2h} axis, which allows one to extract estimated magnitudes for T' for the VO^{2+} defects. For the d_{xy} orbital, there are two solutions to the tensor decomposition, dependent on the relative sign of T′, which cannot be determined from the powder EPR measurement. Nevertheless this gives a reasonable insight into the orbital character of the electron spin density at the vanadium site.

The isotropic hyperfine term, dominated by the Fermi contact interaction, is proportional to the s-character spin density at the nucleus (ρ_s). For VO^{2+}(VLB1), $\rho_s \approx a_{\mathrm{iso}}/A_0 = 0.0682$. Similarly an estimate of the $3d_{xy}$ and $3d_{nz}$ orbital occupancy can also be extracted from the hyperfine values, resulting in values of $\rho_{3d_{xy}} \approx T/(P_{^{51}V} \times 2/7) = 0.905$ and 0.981, and $\rho_{3d_{nz}} \approx T'/(P_{^{51}V} \times 2/7) = 0.0756$. The value for $\rho_{3d_{xy}}$ indicates that the unpaired spin density is almost completely localised on the vanadium site $\left(\sum_i \rho_i = 1.05 \text{ and } 1.12\right)$ with the majority occupying the expected $3d_{xy}$ orbital.

In the case of the high V_2O_5 sample, VLB3, a distinct axial EPR signal is observed lacking any hyperfine structure (Fig. 2). The absence of visible hyperfine arises from a dynamic effect characteristic of the strong exchange narrowing regime, as described by Anderson.[49] In this situation, the exchange frequency is much greater than the rate of modulation caused by the hyperfine or anisotropic exchange interactions. As a result, the time frame of the electron spin relaxation process is sufficiently rapid that the surrounding magnetic framework appears as an effective static field, and therefore the weak

---

‡ Morton and Preston calculate the hyperfine parameters assuming 100% spin density at the interacting nucleus. The isotropic hyperfine parameter, A_0, is obtained by computing $(8\pi g\mu_B\gamma/3)|\psi^2(0)|$ The anisotropic hyperfine parameter, P, was obtained by computing the quantity $P = g\mu_B\gamma\langle r^{-3}\rangle$ assuming $g = g_e$. The full tabulated data for the atomic parameters and angular factors can be obtained here.[48]

perturbation of the energy levels by these effects are effectively averaged. This is further exacerbated by the polaron hopping mechanism, expected in amorphous V_2O_5 materials,[50] due to delocalisation of unpaired spin density across the network.

The local network can be approximated as a distorted V_2O_5-type phase, containing network-modifying $LiBO_2$ units. The nature of the electron transfer for the partially localised spins may be identified by the magnitude of the exchange, with respect to the nearest neighbour $V_V^{\times}$ units, and the activation barrier for hopping conductivity to occur. The dimensionality of the lattice may be determined by the magnitude of the exchange coupling between different lattice dimensions. No resolved structures related to the network modifying VO^{2+} sites found in VLB1 and VLB2 were observed in the VLB3 sample.

The simulated g-values in this strong exchange limit ($J \gg \Delta g\mu_B B$) are characteristic of the mean deviation from g_e, assuming a distribution of magnetic sites arising from distortions in the amorphous framework are present due to variations in the bonding, distance and relative orientation. The mean tetragonality parameter obtained from an average of g_1,g_2 is very high (4.13), indicating a more significant distortion at the V_V' site compared to that observed for VLB1 and VLB2. This is much higher compared to reported values found for other isolated V^{4+} species.[41,42] Clearly, the consequence of the screening of hyperfine and anisotropic (dipolar) exchange interactions is therefore a subsequent loss of information regarding the ground state electronic structure and local environment.

Finally, in the intermediate content sample, VLB2, a rather complex line shape is observed corresponding to a superposition of signals attributed to the network forming (V_2O_5) and network modifying (VO^{2+}) sites identified in VLB3 and VLB1 respectively. An increased broadening of the VO^{2+} signal is consistent with an increased disorder about the isolated sites due to the mixed network-forming phases in the material. Similarly, for the intermediate content glass, VO^{2+} (VLB2) $\rho_s \approx a_{iso}/A_0 = 0.0665$, $\rho_{3d_{nz}} \approx T'/(P_{^{51}V} \times 2/7) = 0.144$ giving solutions $\rho_{3d_{xy}} \approx T/(P_{^{51}V} \times 2/7) = 0.850$ and 0.994. The value for $\rho_{3d_{xy}}$ indicates that the unpaired spin density is again almost completely localised on the vanadium site $\left(\sum_i \rho_i = 1.06 \text{ and } 1.20\right)$, in the ground state $3d_{xy}$ orbital. A notable increase in the d_{nz} contribution was determined in comparison to VO^{2+} (VLB1), which indicated a more significant distortion at the vanadium site in the equatorial plane as the V_2O_5. The majority of the unpaired spin density was still attributed to the ground $3d_{xy}$ orbital.

VT EPR study of the high V_2O_5 content sample (VLB3)

The high V_2O_5 content sample, VLB3, was investigated further using variable temperature (VT) CW EPR between T = 4–370 K, to indirectly probe the electron–electron exchange interactions, and transfer mechanisms responsible for electronic conductivity. The g-anisotropy (and subsequent line shape) is indicative of the inequivalence between exchange and hopping dimensions of the disordered lattice. Ideally, single crystal measurements are necessary to resolve these different contributions to the system. Nevertheless valuable information can still be extracted from the powder spectrum, despite the loss of directional/angular information.

In order to partially recover information on orientational resolution, a phenomenological broadening model was applied to reproduce the changes in line shape as a function of temperature. For cases where the g-anisotropy is non-negligible, it follows that the relaxation time is also orientation-dependent with respect to B_0 which can be approximated by an anisotropic Lorentzian line shape function in the strong-exchange narrowing limit. This likely arises due to the dimensionality of the lattice (coupling along lattice dimensions corresponding to distinct J values), and/or potential antisymmetric Dzyaloshinskii–Moriya (DM) exchange terms (d_{12}) of comparable magnitude to the isotropic integral. This additional term would arise due to the local distortions of the amorphous phase. In the regular, ordered V_2O_5 lattice, the vanadium nuclei possess an inversion centre (assuming no distortion due to Li intercalation or oxygen vacancy formation) which causes the antisymmetric terms to vanish.

The DM exchange interactions are rarely resolved in powder EPR spectra. Single crystal measurements, in conjunction to variable frequency EPR analysis, are often necessary to interrogate this exchange term fully. Although tangible anisotropy between the g_1 and g_2 components is evident, this is comparatively small compared to the g_3 term. This small anisotropy can therefore be neglected in order to obtain orientational information from the rhombic system with respect to the electronic motion and inter-electronic interactions.

In systems with strong isotropic exchange compared to magnetic anisotropy, deviations in the wings of the Lorentzian line shape can occur, producing a line shape that can be approximated by the superposition of broad Gaussian and Lorentzian line shape functions.[51] The observed line shape in the case of VLB3 was thus suitably approximated by a pure Lorentzian function.

The partial ordering in the amorphous system analysed required the use of a suitable ordering potential to simulate the experimental signal intensity. The orientational distribution of the paramagnetic ensemble is non-isotropic and therefore a biased distribution must be calculated.

Due to the nature of the varying linewidths and/or other possible spin Hamiltonian parameters following a change in temperature, each measurement was simulated consecutively by least-squares fitting to obtain approximate parameter fits for the g-values and anisotropic Lorentzian line shape. An ordering potential, λ, was allowed to vary during the initial routine, of the form:

$$P(\theta) = \exp(-U(\theta)) \tag{4}$$

$$U(\theta) = -\lambda\,(3\cos^2(\theta) - 1)/2 \tag{5}$$

which was then averaged and fixed for the second least-squares fitting simulation. Values of $\lambda = -0.7725$ and -0.087 were obtained, respectively, for the temperature ranges T = 4–100 K and 120–370 K, due to the change in orientation of the sample upon switching between spectrometers. These values represent a comparatively weak orientational bias for the amorphous glass within the approximation of a powder sample (where the orientational dependence is not resolved) and thus was a reasonable approximation for the line shape simulations upon variation of the temperature. Several contributions to the linewidth can arise in such complex systems, including the distribution of the *g*-values due to inter-site distortions.

In the strong exchange limit, the relative difference in Zeeman energies represents only a small perturbation to the exchange energy and therefore this effect is expected to be averaged out from the observed line shape. Similarly, the hyperfine and anisotropic exchange interactions that may contribute to unresolved structure within the linewidth are treated as non-perturbing effective fields and also averaged out. Even at temperatures below $T < 50$ K, it was not possible to improve spectral resolution associated with these interactions.

Examples of the fitting results for VLB3 at various temperatures are shown in Fig. 3, and the full set of measurements and simulations at single temperature values, including residual analysis, can be found in the ESI, Fig. S1–S5.† From these simulations, the variation of the average *g*-values, and the peak-to-peak linewidths for the exchange-averaged signal components were determined (where ΔB_{pp} is equivalent to $\Delta B_{\mathrm{pp}} = \Delta B_{\mathrm{FWHM}}/\sqrt{3}$ for the g_3 component), which result from the anisotropic Lorentzian broadening due to the spin relaxation-dominated line width contribution.

The Curie–Weiss behaviour of the EPR magnetic susceptibility is considered by the following equation:

$$\chi_{\mathrm{EPR}} \approx C/(T - \Theta_{\mathrm{CW}})^{\gamma} \tag{6}$$

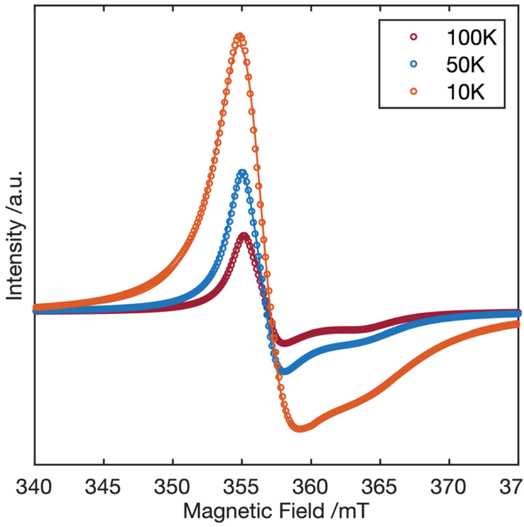

Fig. 3 Example simulations of EPR anisotropic linewidth modelling at single temperature points indicating goodness of fit in the X-band EPR spectrum. The hollow circles correspond to the experimental trace (only 1/8 of the recorded points are shown for clarity). The solid lines correspond to the fitting results using the anisotropic Lorentzian model. The values of the line width and *g*-tensor were obtained from a least-squares fitting routine as a function of temperature.

where χ_{EPR} is the effective EPR magnetic susceptibility, C is the Curie constant, and Θ_{CW} the Curie–Weiss (CW) temperature. γ is a constant usually taken as $\gamma = 1$ in a mean field approach. The EPR temperature dependent peak-to-peak line width can be related to the effective magnetic susceptibility by:[52]

$$\Delta B(T) = [\chi_0(T)/\chi(T)]\Delta B_0^{\infty} \tag{7}$$

where $\chi_0(T)$ is the Curie susceptibility, $\chi(T)$ is the effective susceptibility and ΔB_0^{∞} is the temperature independent contribution to the intrinsic line width.

The EPR line width can be phenomenologically modelled as a linear combination of decomposed components, where $\Delta B_{\mathrm{P}}(T)$ is a function describing the contribution to the linewidth from polaron hopping, and $\Delta B_{\mathrm{CW}}(T)$ is a function describing the Curie–Weiss behaviour:

$$\Delta B(T) = \Delta B_0^{\infty} + \Delta B_{\mathrm{P}}(T) + \Delta B_{\mathrm{CW}}(T) \tag{8}$$

where the temperature-dependent term, $\Delta B_{\mathrm{P}}(T)$:

$$\Delta B_{\mathrm{P}}(T) \propto (1/t_{1\mathrm{e}}(T) + 1/t_{2\mathrm{e}}(T)) \tag{9}$$

includes contributions from spin–spin and spin–lattice relaxation mechanisms. The spin–lattice contribution to the line width was expected to be characteristic of the polaron-hopping motion in the system due to the localisation of spin density at the defect sites and the associated phonon coupling to the lattice.

Values for the experimental line widths were obtained as a function of temperature for a wider range ($T = 4$–370 K). The results are presented in Fig. 4. Both components of the model are represented by distinct temperature regions that characterise the magnetic properties and charge carrier dynamics.

At high temperatures, the line width dependence is approximately linear for both the $g_{1,2}$ and g_3 components respectively, with a similar gradient observed in both cases. Approaching $T = 200$ K, a deviation away from linearity was observed at a minimum linewidth value and corresponding temperature, T_{min}, followed by a plateau over a comparatively long temperature range. Approaching $T = 4$ K, the line width was observed to increase monotonically for both modelled components, albeit *via* different rates. It is not immediately clear as to the contributions to this region due to the competing magnetic and transfer processes as a function of temperature.

It has been reported that, in systems known to undergo polaron hopping, the linewidth exhibits a dependence on the hopping frequency and thus the conductivity.[53] The portion of the experimental data above T_{min} (the value of T for which the minimum linewidth was observed) was therefore fitted to an Arrhenius equation, which describes the $\Delta B_{\mathrm{P}}(T)$ term:[52]

$$\Delta B_{\mathrm{P}}(T) = (A/T)\exp(-E_{\mathrm{a}}/k_{\mathrm{B}}T) \tag{10}$$

where A is a pre-exponential factor, and E_{a} is the activation energy for the hopping process. An excellent fit was afforded for the $g_{1,2}$ components, which accurately reproduced the plateau observed below 200 K. The linear portion of the plot and

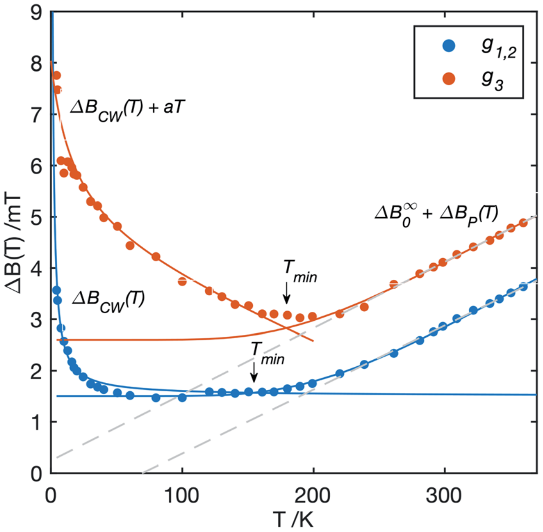

Fig. 4 Results of the linewidth analysis for the $g_{1,2}$ and g_3 components. The lines for the temperature region $T > T_{\text{min}}$ are the result of the fitting to an Arrhenius law (eqn (10)). The lines for the temperature region $T < T_{\text{min}}$ are the result of fitting of the superposition model to the linewidth dependence (eqn (11) and (12), for $g_{1,2}$ and g_3, respectively), after subtracting the contribution from the high temperature Arrhenius type behaviour (Fig. 5). The dashed grey lines provide a representative linear fit. The individual fits are presented in Fig. 5. The parameters obtained from the fits are presented in Table 2.

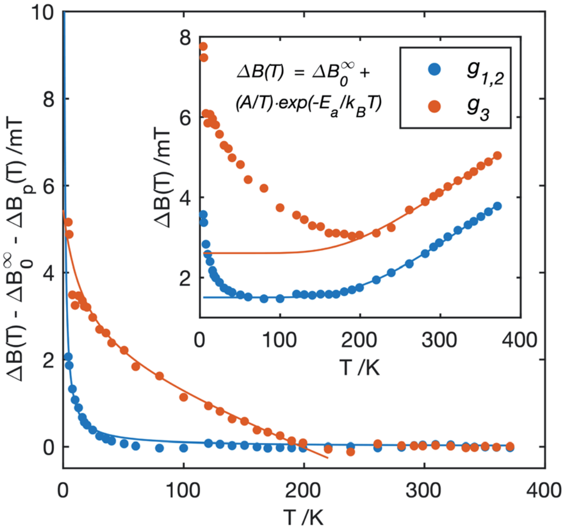

Fig. 5 Line width analysis after subtraction of the polaron hopping contribution to the line width. The fits for the $g_{1,2}$ and g_3 components are defined in eqn (11) and (12). *Inset*: Results for the fit of the Arrhenius law to the total EPR line width temperature dependence, defined in eqn (10).

deviation was well reproduced for the g_3 component. However, the linewidth deviated below T_{min} indicating a further contribution. The fitting afforded values of $\Delta B_0^\infty = 1.390$ mT and $E_a = 0.094$ eV for the $g_{1,2}$ components, and $\Delta B_0^\infty = 2.255$ mT, $E_a = 0.081$ eV for the g_3 component, providing a comparable value for the hopping energy barrier, in agreement with the dependence of the linewidth on the hopping rate. Kosacki *et al.*[54] reported hopping transfer activation energies for $(1 - x)V_2O_g–xLiBO_2$ amorphous glasses in the range $0 < x < 1$ (where $x = 0.2$ for VLB3 in this study) derived from electronic conductivity measurements. The authors reported that the activation energy was minimum in the range $(0 < x < 0.3)$, and the reported values $E_a = 0.10$ eV (for $x = 0.3$) and 0.12 eV (for $x = 0$),[54] are in reasonable agreement with those presented here from EPR line width modelling ($E_a = 0.094$ eV and $E_a = 0.081$ eV).

The linewidth behaviour was then probed at low temperatures, by subtracting the contribution from the polaron hopping conductivity and the intrinsic linewidth, leaving only contributions expected from the Curie–Weiss behaviour, Fig. 5. For the $g_{1,2}$ components, the subtracted line width is effectively zero across most of the temperature range, before increasing asymptotically approaching $T = 0$ K, consistent with paramagnetic Curie–Weiss behaviour where the exchange interaction is zero. The behaviour of the g_3 component, however, is less straight forward, and exhibits a composite behaviour, attributed to two competing processes: (i) an additional apparent linear increase in the line width approaching $T = 0$ K, and (ii) an antiferromagnetic exchange ordering contribution, which results in a monotonic increase in the line width response.

We believe that component (i) corresponds to the transfer of spin density, and its subsequent change in relaxation properties due to the gradual localisation of spin density with decreasing temperature. The low temperature regions ($T < T_{\text{min}}$) were fitted with the following equations for the $g_{1,2}$ components ($\Delta B(T)$):

$$\begin{aligned}\Delta B(T < T_{\min}) &= \Delta B(T) - \Delta B_{\mathrm{P}}(T) - \Delta B_0^\infty = \Delta B_{\mathrm{CW}}(T)\\ &= C/(T - \Theta_{\mathrm{CW}}) \end{aligned} \tag{11}$$

however, to reproduce the linewidth of the g_3 component ($\Delta B'(T)$), an additional contribution was necessary:

$$\Delta B'(T < T_{\min}) = \Delta B(T) - \Delta B_P(T) - \Delta B_0^\infty = \Delta B_{\mathrm{CW}}(T) + aT \tag{12}$$

where C is a constant analogous (but not equal) to the Curie constant, Θ_{CW} is the Curie–Weiss temperature and a is a constant describing the gradient of the superposed linear dependence. Both models reproduced the observed behaviour well for the g-value components, and provided values of $\Theta_{\text{CW}} = -0.005 \pm 5$ K for $g_{1,2}$ (effectively zero within experimental error) and $\Theta_{\text{CW}} = -16.8$ K, $a = -0.01061$ mT K^{-1} for g_3. The isotropic exchange integral may then be estimated from the Curie temperature using the following equation:[49]

$$3k_B\Theta_{\mathrm{CW}} = 2JZS(S + 1) \tag{13}$$

where Z is the number of nearest-neighbour spins, which was kept constant (assuming 2-fold coordination along the hopping dimension) for comparison. The estimated CW temperature values provide values of $J = -0.7928$ cm^{-1} for the g_3 component, and $J = -0.0002$ cm^{-1} for the $g_{1,2}$ components (effectively nil within error). The observed CW behaviour is therefore convincing proof that the VLB3 glass possesses a one-dimensional hopping pathway (and hence one-dimensional exchange lattice), with a moderate antiferromagnetic coupling, and a virtually paramagnetic (uncoupled) behaviour along the other dimensions. We may consider that the broad g_3 component is aligned to the dimension of the hopping conduction which would correspond with a decrease in the spin relaxation time due to the antiferromagnetic coupling.

The spin–lattice relaxation time, $t_{1\mathrm{e}}$, is expected to be comparable to the order of the spin–spin relaxation time, $t_{2\mathrm{e}}$, along the hopping dimension due to the strong coupling of the spin-phonon modes. The orientation of the g_3 component with respect to the crystallographic domain was therefore expected to coincide with the shortest V–V distance and the hopping dimension, as depicted in Fig. 1. The fit of the Arrhenius law (Fig. 5) showed that the effective hopping frequency, below the critical temperature, tends towards a linear dependence as the temperature was decreased.

In this situation, the phonon modulation of the lattice is coincident not only with the spin–lattice relaxation processes, but also the localisation of spin density at the trapping defect sites.[55] We propose that for the region $T < T_{\mathrm{min}}$, the polarisation of the conduction electron spin density increases substantially due to the introduction of orbital angular momentum into the spin–orbit coupling and subsequent effective magnetic moment, in addition to spin–spin relaxation contributions that are proportional to the spin density at the site, due to the Fermi contact, isotropic and anisotropic exchange contributions. The effect of spin localisation is therefore observed as an increase in the effective magnetic moment at the electronic site due to spin–orbit and spin–spin coupling contributions. Assuming that this effect is dominated by $t_{1\mathrm{e}}$, the linear behaviour suggests the contribution is associated with a one-phonon relaxation process, which usually dominates at high temperatures and has the opposite gradient. We therefore tentatively propose that the apparent linear contribution corresponds to the effective spin density at the V_V' trapping sites, where spin–orbit coupling is non-negligible.

The behaviour of the g-tensor over the temperature range $T =$ 4–370 K was also investigated and is presented in Fig. 6. The apparent g values are shifted away from free-spin by the spin–orbit coupling, and therefore any change in these values is characteristic of a change of the local electronic environment. At high temperatures, a quasi-axial symmetry is observed with two inequivalent components. However, upon lowering of the temperature, the $g_{1,2}$ components diverge, exhibiting an asymmetry that is central to the averaged value at high temperatures. This averaging is attributed to the effective screening of the magnetic anisotropy between the g_1,g_2 components due to the hopping transfer, which occurs on a timescale less than or comparable to $t_{1\mathrm{e}}$.[56] Across most of the temperature range, the values remain effectively constant, until they diverge significantly approaching $T = 4$ K. The anisotropy between the g_1 and g_2 components, and additionally between the $\langle g_1 + g_2 \rangle$ and g_3 components, increases dramatically.

This divergence provides further convincing evidence of the localisation of spin density, and subsequent increase in the spin–orbit and spin–spin coupling interactions, which was attributed to the linear dependence in the linewidth at low temperatures. The isotropic g-value deviates also to a slightly lower value, which is expected to be characteristic of the increasing population of the V_V' sites formed *via* Li incorporation/oxygen vacancy formation.

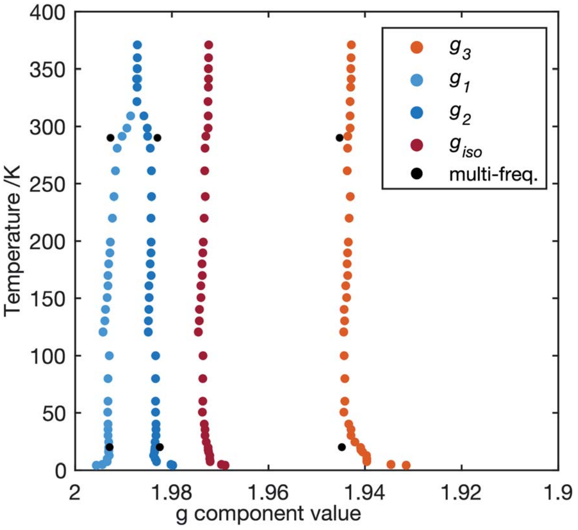

Fig. 6 Results of g-tensor monitoring obtained from the variable temperature modelling. The filled black circles are the results from the simultaneous multiple frequency fitting at $T = 20$ K (and $T = 10$ K for Q-band) and $T = 290$ K at X- and W-band frequencies (see ESI: Fig. S7†).

The effect of anisotropic exchange can similarly shift the g-value as a function of temperature due to the mixing of excited states *via* spin–orbit coupling.[51] This effect also likely contributes an important role in the inter-electronic coupling mechanism, however this is difficult to probe in the situation of a disordered system. Finally, the observed deviation of the g-values illustrates the averaging of disorder within the system due to exchange and hopping processes.

Concerning the nature of the exchange coupled states, comparing back to the schemes presented in eqn (1) and (2), the V_V' site observed in VLB3 is attributed to the redistribution of charge carriers due to the incorporation of primary oxygen vacancy defects (1), rather than by Li incorporation from the minor phase, although these are likely to contribute significantly to the electronic conductivity also.

Variable frequency EPR of the high V_2O_5 content sample (VLB3)

The line shape and structure of the VLB3 sample was further investigated at multiple EPR measurement frequencies, in order to better resolve the g-tensor components. The resulting X-, Q- and W-band EPR spectra, recorded at $T = 20$ K (X-, W-band) and $T = 10$ K (Q-band), are presented in Fig. 7. The variation of the line width, and values of g, was determined to be less than 5% (within error) at the two temperatures. At Q- and W-band frequencies, a rhombic g-tensor can be readily identified, which are characteristic of the inequivalent equatorial directions possessed by sites of orthorhombic symmetry. A dominant Lorentzian line shape persists in these spectra,

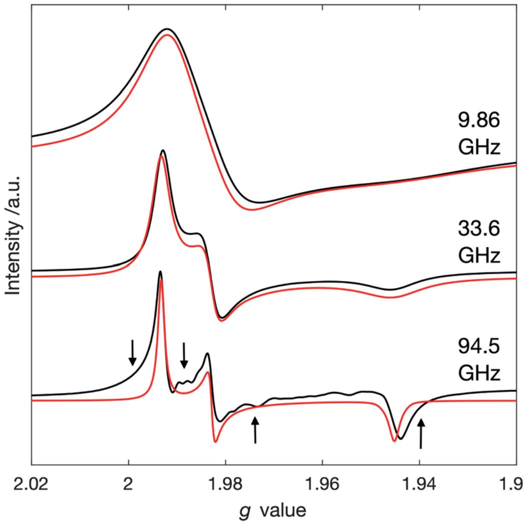

Fig. 7 CW EPR spectra of the V_2O_5–$LiBO_2$ sample (VLB3) collected at X- (9.5 GHz), Q- (35 GHz) and W-band (95 GHz) frequencies, plotted on the g-scale for ease of comparison. The black arrows indicate regions of the W-band spectrum, which were not reproduced by the simulation, which are thought to arise from disorder at the vanadium trapping sites.

particularly at X-band. This can be attributed to the anisotropic spin relaxation processes resulting from g anisotropy (Zeeman effect) and exchange coupling along the lattice dimensions in the strong exchange limit,[57] where additional contributions to the line width (such as distributions of g and A) are effectively screened. The X-, Q- and W-band EPR spectra were simulated and fitted by taking into consideration the line width anisotropy and averaged resonant field positions for the exchange-coupled V^{4+} site. The spin Hamiltonian used for simulation of the single dimension with two nearest neighbours, was of the form:

$$\hat{H} = \sum_i g_i \mu_B B \hat{s}_i - 2J \hat{s}_i \cdot \hat{s}_j \qquad (14)$$

Using this equation, any possible nuclear, hyperfine, anisotropic or antisymmetric exchange contributions, which were not resolved from the spectrum, were neglected in the simulation. Even the difference in Zeeman energies is effectively averaged along the hopping direction, and therefore the intersite disorder was not considered. For the W-band spectrum, it was necessary to include an additional simulation parameter to correct for the microwave phase, which is non-zero, although this was comparatively small.

The g_1 and g_2 anisotropy was already clearly resolved in the Q-band spectrum, thereby confirming the modelling results presented earlier based on the X-band measurements alone, where this anisotropy was not immediately resolved. The g-tensor parameters obtained from the simulations (those presented in Table 1 and Fig. 7) were in good agreement with similar amorphous systems possessing a square pyramidal V^{4+} symmetry.[42,58] While the deviation of the obtained g values from the relatively constant positions above T = 20 K may be overestimated, this is nevertheless an indication of the increase in anisotropy between the g_1, g_2, and g_3 turning points in the powder EPR spectrum. A series of weakly resolved features were also detected between the g_1 and g_3 components in the W-band spectrum (Fig. 7). Their origin is unclear, and could arise from a number of factors, including distortions of the exchange-coupled sites away from co-linear orientations, residual hyperfine structure arising from trace concentrations of VO^{2+} phases observed in VLB1, and distinct, exchange-coupled species relating to unpaired electrons at the vanadium, oxygen, or vacancy sites.

The apparent linewidth of the g_3 component was observed to decrease on the g-scale (similar to the g_1, g_2 components) with increasing frequency. The fact that a frequency independent linewidth was observed is also consistent with the explanation that the line broadening is relaxation-dominated. Several additional (frequency-independent) sources of broadening are possible for real, low dimensional systems such as unresolved hyperfine coupling, anisotropic and antisymmetric exchange contributions, g anisotropy and crystal field effects.[59] The fact that angularly resolved measurements in a defined coordinate frame is not possible here, complicates the process of determining which broadening mechanism occurs. None of these interactions were resolved across the entire temperature range studied here. Therefore, we suggest that the anisotropic linewidth arising from spin relaxation is a suitable model for the observed line broadenings effects in the VLB3 sample.

Another interesting feature not reproduced by the simulation are the asymmetric shoulders to low and high field of the g_1 and g_3 components (Fig. 7). At $T = 20$ K, increased anisotropy in the signal is apparent. The simulated Lorentzian line shape corresponds well to the centre of the turning points of the spectrum, and in contrast, diverges asymmetrically within the wings of the line shape. This anisotropic line shape is attributed to the orientational disorder due to variations in the bond angle and length between random defect sites within the disordered network. As the hopping frequency tends to zero, this orientational strain would become more apparent, which would modulate the value of g with a probability distribution rapidly vanishing towards the wings of the signal.

Conclusions

A series of V_2O_5–$LiBO_2$ mixed conductive glasses (abbreviated VLB1–3) were investigated using CW EPR spectroscopy. At low V_2O_5 content (sample VLB1), an isolated $S = \frac{1}{2}$ vanadium defect centre was identified at a network modifying position within the $LiBO_2$ matrix. The observed spin Hamiltonian parameters were consistent with a V^{4+} centre possessing a distorted octahedral configuration, with the spin density primarily localised in the d_{xy} ground state orbital.

At high V_2O_5 content (sample VLB3), a distinct exchange-narrowed signal was observed. This observation is consistent with the presence of a strongly polarised CESR/one-dimensional exchange-coupled lattice possessing a distorted square pyramidal geometry (*i.e.*, can be considered *ca.* V_2O_5 to short-range order). The species responsible for this site likely arises from defects formed from intrinsic oxygen vacancies within the disordered network, although the Li intercalation defect site is also likely to be a significant contribution.

Linewidth and g-tensor analysis of the EPR signals in VLB3 evidenced a marked temperature dependent behaviour, consistent with a polaron hopping mechanism of electron transfer and inter-electronic exchange along the g_3 direction, which was proposed to be coincident with the electron transfer axis. At temperatures approaching the minimum observed line width, $T_{\min}$, a deviation away from linear behaviour was observed, coincident with a dominant contribution from the hopping process. The activation energy (E_a) was estimated to be 0.081 eV which is consistent with other conducting glass systems. Separation of the underlying line width contributions were achieved based on a superposition model (including the Curie–Weiss law). The analysis identified contributions from exchange interactions and an additional process for the g_3 component, which was attributed to the spin–orbit and spin–spin contributions to the relaxation upon transition to a localised state.

Finally, a relaxation-dominated line broadening mechanism was further supported by multi-frequency EPR measurements, which also identified unresolved features at high frequencies due to unaccounted for anisotropic exchange/speciation within the disordered network. This analysis provides a straightforward method for the use of EPR to investigate solid-state glassy materials, and to understand their functional properties.

Conflicts of interest

The authors declare no conflicts of interest.

Acknowledgements

The authors thank the EPSRC and Johnson Matthey for funding JS (through an iCASE award) and EPSRC for the grant EP/P019951. Information on the data underpinning the results presented here, including how to access them, can be found in the Cardiff University data catalogue at http://doi.org/10.17035/d.2021.0138004794.

Notes and references

1 L. Li, Q. Shao and X. Huang, *Chem.–Eur. J.*, 2020, **26**, 3943–3960.

2 S. Anantharaj and S. Noda, *Small*, 2020, **16**, 1905779.

3 Y.-C. Hu, C. Sun and C. Sun, *ChemCatChem*, 2019, **11**, 2401–2414.

4 S.-H. Lee, H. M. Cheong, M. J. Seong, P. Liu, C. E. Tracy, A. Mascarenhas, J. R. Pitts and S. K. Deb, *J. Appl. Phys.*, 2002, **92**, 1893.

5 K. I. Cho, S. H. Lee, K. H. Cho, D. W. Shin and Y. K. Sun, *J. Power Sources*, 2006, **163**, 223–228.

6 K. Cho, T. Lee, J. Oh and D. Shin, *Solid State Ionics*, 2007, **178**, 119–123.

7 M. Helena Braga, A. J. Murchison, J. A. Ferreira, P. Singh and J. B. Goodenough, *Energy Environ. Sci.*, 2016, **9**, 948–954.

8 N. B. Wyatt and M. W. Liberatore, *Soft Matter*, 2010, **6**, 3346–3352.

9 R. Komiya, A. Hayashi, H. Morimoto, M. Tatsumisago and T. Minami, *Solid State Ionics*, 2001, **140**, 83–87.

10 C.-H. Lee, K. H. Joo, J. H. Kim, S. G. Woo, H.-J. Sohn, T. Kang, Y. Park and J. Y. Oh, *Solid State Ionics*, 2002, **149**, 59–65.

11 S. Afyon, F. Krumeich, C. Mensing, A. Borgschulte and R. Nesper, *Sci. Rep.*, 2014, **4**, 7113.

12 Y. Sakurai, T. Hirai, S. Okada, T. Okada, J.-i. Yamaki and H. Ohtsuka., *US Pat.*, US4675260A, 1987.

13 M. Inamoto, H. Kurihara and T. Yajima, *Electrochemistry*, 2012, **80**, 421–422.

14 T. S. Arthur, K. Kato, J. Germain, J. Guo, P.-A. Glans, Y.-S. Liu, D. Holmes, X. Fan and F. Mizuno, *Chem. Commun.*, 2015, **51**, 15657–15660.

15 A. Konarov, H. J. Kim, J.-H. Jo, N. Voronina, Y. Lee, Z. Bakenov, J. Kim and S.-T. Myung, *Adv. Energy Mater.*, 2020, **10**, 2001111.

16 J. Faucheu, E. Bourgeat-Lami and V. Prevot, *Adv. Eng. Mater.*, 2019, **21**, 1800438.

17 N. Johnson, G. Wehr, E. Hoar, S. Xian, U. Akgun, S. Feller, M. Affatigato, J. Repond, L. Xia, B. Bilki and Y. Onel, *Int. J. Appl. Glass Sci.*, 2015, **6**, 26–33.

18 J. H. Perlstein, *J. Solid State Chem.*, 1971, **3**, 217–226.

19 A. K. Bandyopadhyay, J. O. Isard and S. Parke, *J. Phys. D: Appl. Phys.*, 1978, **11**, 2559–2576.

20 D. Maniu, T. Iliescu, I. Ardelean, I. Bratu and C. Dem, *Stud. Univ. Babes-Bolyai, Phys.*, 2001, 366–371.

21 O. Cozar, I. Ardelean, I. Bratu, S. Simon, C. Craciun, L. David and C. Cefan, *J. Mol. Struct.*, 2001, **563–564**, 421–425.

22 Z. Ren Xiao, G. Yu Guo, P. Han Lee, H. Shu Hsu and J. Chun Andrew Huang, *J. Phys. Soc. Jpn.*, 2008, **77**, 023706.

23 D. Dreifus, M. P. F. Godoy, A. C. Rabelo, A. D. Rodrigues, Y. G. Gobato, P. C. Camargo, E. C. Pereira and A. J. A. de Oliveira, *J. Phys. D: Appl. Phys.*, 2015, **48**, 445002.

24 K. McColl, I. Johnson and F. Corà, *Phys. Chem. Chem. Phys.*, 2018, **20**, 15002–15006.

25 K. E. Swider-Lyons, C. T. Love and D. R. Rolison, *Solid State Ionics*, 2002, **152–153**, 99–104.

26 J. Krzystek, A. Ozarowski, J. Telser and D. C. Crans, *Coord. Chem. Rev.*, 2015, **301–302**, 123–133.

27 M. Farouk, K. Abdallauh, M. Attallah and Z. M. Abd El-Fattah, *J. Non-Cryst. Solids*, 2019, **523**, 119607–119607.

28 S. Khasa, M. S. Dahiya, A. Agarwal and P. Chand, *J. Mol. Struct.*, 2015, **1079**, 15–20.

29 D. Mustafi, E. V. Galtseva, J. Krzystek, L. C. Brunel and M. W. Makinen, *J. Phys. Chem. A*, 1999, **103**, 11279–11286.

30 T. Aoyagi, S. Kohara, T. Naito, Y. Onodera, M. Kodama, T. Onodera, D. Takamatsu, S. Tahara, O. Sakata, T. Miyake, K. Suzuya, K. Ohara, T. Usuki, Y. Hayashi and H. Takizawa, *Sci. Rep.*, 2020, **10**, 7178.

31 N. S. Saetova, A. A. Raskovalov, B. D. Antonov, T. V. Yaroslavtseva, O. G. Reznitskikh, E. V. Zabolotskaya, N. I. Kadyrova and A. A. Telyatnikova, *Ionics*, 2018, 1–10.

32 A. Gaddam, A. R. Allu, H. R. Fernandes, G. E. Stan, C. C. Negrila, A. P. Jamale, F. O. Méar, L. Montagne and J. M. F. Ferreira, *J. Am. Ceram. Soc.*, 2021, **104**, 2495–2505.

33 S. Stoll and A. Schweiger, *J. Magn. Reson.*, 2006, **178**, 42–55.

34 P. Pietrzyk and Z. Sojka, *Appl. Magn. Reson.*, 2011, **40**, 471–479.

35 S. Grasser, C. Haeßner, K. Köhler, F. Lefebvre and J.-M. Basset, *Phys. Chem. Chem. Phys.*, 2003, **5**, 1906–1911.

36 M. Chiesa, V. Meynen, S. Van Doorslaer, P. Cool and E. F. Vansant, *J. Am. Chem. Soc.*, 2006, **128**, 8955–8963.

37 V. Nagarajan, B. Müller, O. Storcheva, K. Köhler and A. Pöppl, *Res. Chem. Intermed.*, 2007, **33**, 705–724.

38 V. Luca, † D. J. MacLachlan and R. Bramley, *Phys. Chem. Chem. Phys.*, 1999, **1**, 2597–2606.

39 J. E. Garbarczyk, L. Tykarski, P. Machowski and M. Wasiucionek, *Solid State Ionics*, 2001, **140**, 141–148.

40 O. Cozar, I. Ardelean and Gh. Ilonca, *Mater. Chem.*, 1982, **7**, 755–765.

41 Y. H. Kim, T. H. Noh, J. P. Kang, S. D. Hong, D. Choi and S. K. Song, *J. Korean Phys. Soc.*, 2013, **62**, 906–911.

42 C. S. Sunandana and A. K. Bhatnagar, *J. Phys. C: Solid State Phys.*, 1984, **17**, 467.

43 A. Sheoran, A. Agarwal, S. Sanghi, V. P. Seth, S. K. Gupta and M. Arora, *Phys. B*, 2011, **406**, 4505–4511.

44 V. P. Seth, A. Yadav and P. Chand, *J. Non-Cryst. Solids*, 1987, **89**, 75–83.

45 G. L. Narendra, J. Lakshmana Rao and S. V. J. Lakshman, *Solid State Commun.*, 1991, **77**, 235–237.

46 D. Sreenivasu, N. Narsimlu, G. S. Sastry and V. Chandramouli, *Phys. Status Solidi A*, 1994, **143**, K107–K110.

47 D. Kivelson and S.-K. Lee, *J. Chem. Phys.*, 2004, **41**, 1896.

48 J. R. Morton and K. F. Preston, *J. Magn. Reson.*, 1978, **30**, 577–582.

49 P. W. Anderson and P. R. Weiss, *Rev. Mod. Phys.*, 1953, **25**, 269–276.

50 L. Murawski, C. Gledel, C. Sanchez, J. Livage and J. P. Audières, *J. Non-Cryst. Solids*, 1987, **89**, 98–106.

51 A. Zorko, in *Topics From EPR Research*, ed. A. M. Maghraby, IntechOpen, 2019.

52 S. K. Misra, S. I. Andronenko, S. Asthana and D. Bahadur, *J. Magn. Magn. Mater.*, 2010, **322**, 2902–2907.

53 H. Mori, *Prog. Theor. Phys.*, 1965, **33**, 423–455.

54 I. Kosacki, M. Massot, M. Balkanski and H. L. Tuller, *Mater. Sci. Eng., B*, 1992, **12**, 345–349.

55 V. I. Krinichnyi, P. A. Troshin and N. N. Denisov, *J. Chem. Phys.*, 2008, **128**, 164715.

56 A. Aguirre, P. Gast, S. Orlinskii, I. Akimoto, E. J. J. Groenen, H. E. Mkami, E. Goovaerts and S. V. Doorslaer, *Phys. Chem. Chem. Phys.*, 2008, **10**, 7129–7138.

57 S. Schott, E. R. McNellis, C. B. Nielsen, H.-Y. Chen, S. Watanabe, H. Tanaka, I. McCulloch, K. Takimiya, J. Sinova and H. Sirringhaus, *Nat. Commun.*, 2017, **8**, 15200.

58 E. Gillis and E. Boesman, *Phys. Status Solidi B*, 1966, **14**, 337–347.

59 A. Bencini and D. Gatteschi, *Electron Paramagnetic Resonance of Exchange Coupled Systems*, Springer-Verlag, Berlin Heidelberg, 1990.